The International Journal of Advanced Manufacturing Technology (2025) 141:1523–1538
https://doi.org/10.1007/s00170-025-16752-9

ORIGINAL ARTICLE

Galvanic interactions between SLM-built and cast aluminium alloy interfaces in hybrid structures: a microstructural and electrochemical study

Samson Dare Oguntuyi[1] · Mandlenkosi G. R. Mahlobo[2] · Ngeleshi M. Kibambe[1] · Kasongo Nyembwe[3] · Peter M. Mashinini[4] · Peter Apata Olubambi[1]

Received: 1 August 2025 / Accepted: 1 October 2025 / Published online: 18 October 2025

Abstract
Hybrid aluminium configurations, consisting of selective laser melting (SLM)-built regions incorporated with traditionally cast substrates, give outstanding prospects for tailored functional and mechanical performance. This study examines the galvanic corrosion performance of aluminium hybrid systems comprising SLM-built regions of varying compositions on cast substrates. The electrochemical evaluations, such as open circuit potential (OCP), potentiodynamic polarization (PDP), and electrochemical impedance spectroscopy (EIS), were carried out in a 1 M hydrochloric acid (HCl) solution to determine the galvanic coupling across the built–substrate interface, supported by SEM/EDS and XRD analyses. Outcomes showed that galvanic performance was hugely affected by both microstructural alterations and local compositional rising, with greater silicon content in the SLM section initiating the development of cathodic intermetallic phases that deepened localized anodic dissolution in the nearby cast matrix. The corresponding cast substrate with refined passive layers showed greater resistance to galvanic attack, whereas galvanic current was significantly higher at interfaces comprising SLM regions with higher Si content. These discoveries emphasize the necessity of microstructural compatibility and organized compositional changes in reducing galvanic corrosion in hybrid aluminium systems, thereby supporting their engagement in aerospace and marine environments.

Keywords Galvanic corrosion · Hybrid aluminium · Selective laser melting · Casting · Chloride environment

1 Introduction

Aluminium and its alloys remain foundational in aerospace, automotive, marine, and structural applications due to their outstanding combination of light weight, mechanical strength, corrosion resistance, and workability [1, 2]. Among these features, corrosion resistance is a major concern for service reliability, specifically in harsh environments like industrial atmospheres, seawater, or regions where de-icing salts are often used [3]. Although aluminium normally develops a passive oxide layer (Al_2O_3) that shields it from further oxidation, this film becomes progressively susceptible in chloride-containing solutions, where pitting and localized attacks often originate [4].

One of the most insidious types of corrosion under such circumstances is galvanic corrosion, which occurs when two sections of varying electrochemical potential are electrically coupled in an electrolyte. Though this mechanism is normally linked with dissimilar metals, galvanic corrosion can

✉ Samson Dare Oguntuyi
samsoniumdare@gmail.com

1 Centre for Nanoengineering and Advanced Materials (CeNAM), School of Mining, Metallurgy and Chemical Engineering, University of Johannesburg, Johannesburg 2092, South Africa

2 Department of Chemical and Materials Engineering, University of South Africa, P.O. Box 392, Florida 1709, South Africa

3 Department of Mechanical and Mechatronic Engineering, Cape Peninsula University of Technology, Cape Town, South Africa

4 Department of Mechanical and Industrial Engineering, University of Johannesburg, Doornfontein Campus, Johannesburg 2028, South Africa

Fig. 1 Fabricated hybrid aluminium samples with labeled descriptions highlighting the SLM-built region, the hybrid interface, and the cast substrate

similarly occur within the same base metal if there are local variations in the composition, microstructure, or processing history, which is an increasingly important concern in the era of hybrid manufacturing. Recently, there has been huge attention paid to hybrid materials configuration that associates additive manufacturing (AM) methods, like selective laser melting (SLM), with conventional casting [5, 6]. This combination gives modern prospects to enhance functionality, minimize waste, and customize design. For example, intricate sections of a part can be additively manufactured with tailored microstructures and geometries, while the whole structure can be developed through economical casting. However, such hybridization incorporates surface chemistry and microstructure variation, specifically at the interface between the built and cast zones [7]. These differences can develop electrochemical gradients, leading to the emergence of microgalvanic cells and localized corrosion [6]. A pronounced interesting case is that of aluminium–silicon hybrid systems. The SLM technique, featured by quick solidification, often produces a homogeneous and fine-grained densely packed microstructure with higher mechanical and corrosion resistance than its cast counterpart [8]. On the other hand, cast aluminium tends to show microsegregated intermetallics, coarser dendritic grains, and increased porosity, characteristics that are intrinsically more prone to corrosion [9]. When these two regions are merged in a hybrid system, their microstructural and electrochemical variations can form galvanic correlation, particularly in chloride-containing media like NaCl or HCl [10, 11].

Some works have established the corrosion performance of either additively manufactured (AM) aluminium alloys or conventionally cast alloys [12–14]; examinations into galvanic interactions at the interface of hybrid configurations, where AM and cast sections are combined, have similarly received some consideration [15–18]. Remain rarely exploited is the electrochemical gradient across the AM–cast boundary in certain types of hybrid structures comprising varieties of Al alloys examined under the same condition. This is an important oversight, particularly considering hybrid structures are increasingly adopted in applications like aerospace component refurbishment, marine systems integration, and multifunctional lightweight assemblies. Unlike conventional dissimilar metal coupling, these hybrids incorporate localized galvanic dangers owing to subtle yet huge variances in microstructure, composition, and processing-induced surface states within the same alloy structures. Addressing this specific corrosion mechanism is paramount for ensuring long-term dependability and structural integrity in next-generation metallic structures.

However, few works have studied the galvanic effects at SLM-cast hybrid aluminium interfaces under chloride environments. Through the engagement of electrochemical characterization methods, such as open circuit potential (OCP), electrochemical impedance spectroscopy (EIS), and potentiodynamic polarization (PDP), the corrosion kinetics and galvanic tendencies between zones were investigated. Also, surface and phase characterization through scanning electron microscopy (SEM), X-ray diffraction (XRD), and energy-dispersive X-ray spectroscopy (EDS) gives an understanding of corrosion morphology and by-product development. The findings of this research aim to establish a stronger clarity of how processing method, elemental dispersal, and microstructural enhancement (specifically Si composition and others) influence galvanic performance in aluminium hybrid configurations. These understandings are important for enhancing the practical application of hybrid manufacturing technologies in corrosion-related environments, while also adding meaningfully to the continuing discourse on metallurgical compatibility within modern engineered material systems.

2 Materials and methods

2.1 Fabrication of hybrid aluminium samples

Three hybrid aluminium samples were fabricated via selective laser melting (SLM) and bonded to cast aluminium substrates to form built–substrate systems (Fig. 1). Sample A comprised an Al–Si7 built region on cast Al 6061, Sample B used Al–Si10 on Al 6061, and Sample C combined Al–Si7 with cast Al 5083. The built regions

Table 1 Chemical composition (wt%) of SLM-built and substrate aluminium alloys used in hybrid configurations

Alloys	Elements								
	Fe	Ti	Cu	Cr	Mn	Zn	Mg	Si	Al
Al 7 (wt%)	0.40	0.16	0.25	0.11	0.10	0.50	0.40	7.00	Remaining
Al 10 (wt%)	0.10	0.18	0.25	0.40	0.05	0.50	0.10	10.00	Remaining
Al 6061 (wt%)	0.70	0.15	0.40	0.30	0.15	0.20	1.00	0.80	Remaining
Al 5083 (wt%)	0.40	0.15	0.1	0.35	0.40	0.25	4.9	0.40	Remaining

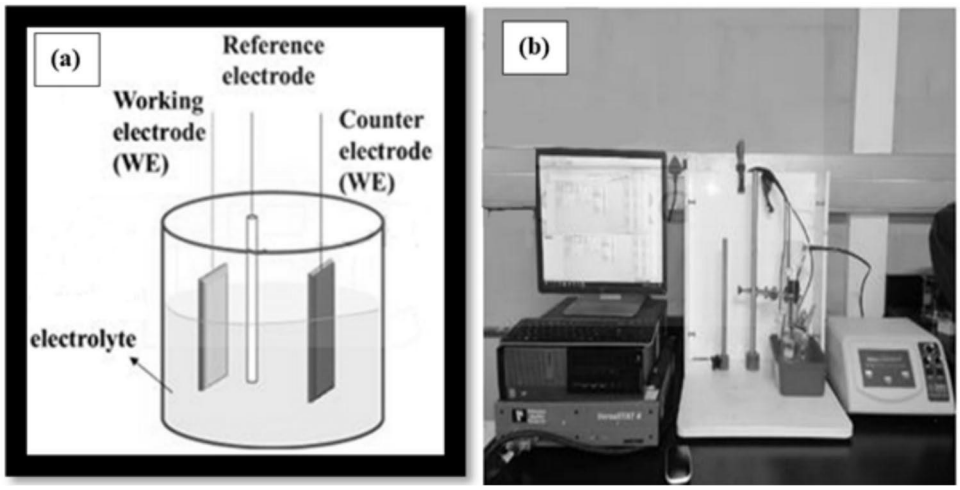

Fig. 2 Illustration of **a** the experimental setup, and **b** the electrode configuration connected to the potentiostat system

were formed using gas-atomized Al–Si pre-alloyed powders, and the SLM process ensured high-density parts with sound metallurgical interfaces. These combinations were selected to assess the effects of silicon content and substrate type on microstructural features and corrosion behaviour.

Before SLM deposition, cast substrates were machined to a flatness of ± 0.05 mm. SLM was performed using a fiber laser-based powder bed system with a laser power of 350 W, scan speed of 1200 mm/s, hatch spacing of 110 µm, and layer thickness of 30 µm. These parameters were chosen to optimize density and minimize porosity. After fabrication, the coupled built and cast regions were sectioned into standardized specimens (approximately 10 mm × 10 mm) for electrochemical testing, ensuring consistency and reproducibility across test conditions. Care was ensured to isolate the specific zones (the coupled SLM-built and cast substrate) for targeted corrosion evaluation, ensuring consistency and reproducibility across test conditions. Each experiment was conducted in triplicate to validate the reliability of the results. The schematic illustration of the hybrid configuration is provided in Fig. 1, while the chemical compositions of the build and substrate materials (aluminium alloys) are stated in Table 1, providing a clear background for the subsequent analysis of the microstructural and electrochemical behaviour of the hybrid aluminium components.

2.2 Microstructural characterization

Prior to corrosion examination, all samples were prepared metallographically using standard grinding and polishing procedures to attain a mirror-like surface finish. The specimens were then etched using Keller's reagent to reveal their underlying microstructural features. Surface morphology and compositional analysis were performed using scanning electron microscopy (SEM) coupled with energy-dispersive X-ray spectroscopy (EDS) (JEOL, operated at 15 kV).

Also, X-ray diffraction (XRD) was employed with post-exposure using Cu-Kα radiation over a 2θ range of 10°–90°. For the post-corrosion analysis, the SEM with EDS was applied to observe the morphology of the corrosion-affected samples and pitting patterns, as well as the corrosion products, which thus aided in understanding the degradation mechanisms across the hybrid zones.

2.3 Electrochemical testing

Electrochemical measurements were carried out in a 1 M hydrochloric acid (HCl) solution so as to determine the corrosion behaviour of the hybrid aluminium systems. The solution was prepared with deionized water and sustained at normal temperature (~ 25 °C). A standardized three-electrode arrangement was used for all the examinations: Fig. 2 shows the electrochemical setup, including the experimental

arrangement and electrode configuration used for the measurements. A standard three-electrode setup was employed for all tests:

- Working electrode: The coupled regions, consisting of both the SLM-built and cast substrate zones, were embedded in epoxy resin, with only the particular area of interest (the combined built and substrate region) exposed to the electrolyte. The exposed surface area was carefully controlled to approximately 1 cm^2 to ensure consistent electrochemical testing.
- Reference electrode**:** A Saturated Calomel Electrode (SCE) was applied to give a stable and reliable reference potential throughout the tests.
- Counter electrode: A high-purity graphite rod served as the counter electrode, offering good conductivity and chemical stability during the electrochemical tests.

All tests were performed using a computer-controlled potentiostat (Gamry Instruments).

2.3.1 Open circuit potential (OCP)

OCP was recorded uninterruptedly for a 2-h duration to observe the initial electrochemical stability of the coupled parts. This ensured the system reached a steady-state potential and provided a thermodynamic reference point for subsequent tests.

2.3.2 Potentiodynamic polarization (PDP)

Potentiodynamic polarization scans were conducted in the range of –250 mV below the OCP to + 500 mV above it at a scan rate of 0.667 mV/s. The Tafel extrapolation method was applied to determine the corrosion potential (E_{corr}) and corrosion current density (I_{corr}) and ultimately calculate the corrosion rate using the following standard equation:

$$\text{Corrosion Rate (mm/year)} = \frac{K.I_{corr}.EW}{\rho}$$

where:

- $\mathbf{K} = 3.27 \times 10^{-3}$ mm·g/μA·cm·year (unit conversion constant),
- $\mathbf{I_{corr}}$ is in μA/cm^2,
- **EW** = Equivalent weight of aluminium
- **ρ** = Density of aluminium (~ 2.7 g/cm^3).

This technique provided valuable quantitative insights into the corrosion kinetics of both the built and substrate regions, helping to determine which zone behaved more anodically and which acted as the nobler (cathodic) component during the electrochemical procedure.

2.3.3 Electrochemical impedance spectroscopy (EIS)

EIS measurements were carried out at the stabilized OCP to evaluate the electrochemical performance over the range of frequencies. The impedance spectra were achieved from 100 kHz to 10 mHz via a 10 mV AC perturbation.

Nyquist and Bode plots were analyzed to interpret the charge transfer resistance and passive film characteristics. The impedance data were fitted to appropriate equivalent circuit models using EC-Lab, which yielded values for polarization resistance (R_p), film capacitance, and other relevant parameters such as constant phase elements (CPE). This approach enabled a deeper understanding of the corrosion protection mechanisms active in the coupled parts relative to one another.

3 Results and discussion

3.1 Microstructural characterization of As-fabricated hybrid samples

The microstructures of the hybrid aluminium alloy samples, prior to corrosion exposure, provide foundational insight into the material integrity and interfacial bonding of the built and substrate regions. Each hybrid consists of a selective laser melted (SLM) aluminium–silicon alloy deposited onto a cast aluminium alloy substrate, making a metallurgically bonded hybrid bi-material structure. Although Al and Si are the major elements in the built sections, small amounts of other elements, like Fe, Mg, Cu, Zn, and Cu, are also present. Despite their relatively lesser concentrations, these minute elements affect secondary phase development and local microstructural changes, particularly in the interfacial zones and melt pool boundaries [19]. Also, the interfacial and phase dispersal features play an important role in examining the galvanic and corrosion behaviour of these hybrids.

Figure 3a depicts sample A, which has an Al-Si7 SLM built over a cast Al 6061 substrate. A form of fine-cellular-dendritic structure is revealed in the additively manufactured section. The associated rapid cooling with the SLM process enhances the microstructure and causes a uniform dispersal of silicon along the cell boundaries as part of the Al-Si eutectic. The existence of minute amounts of iron and magnesium definitely adds to the development of intermetallic compounds like AlFeSi and Mg_2Si (as depicted in the XRD – Fig. 5), slightly improving local hardness and affecting corrosion paths [20]. On the substrate side, the cast Al 6061 shows a coarser dendritic morphology with erratic porosity and huge intermetallic inclusions, features consistent with conventional casting [21]. At the fusion boundary, a progressive microstructural change is observed, with no visible voids or cracks, reflecting a steady metallurgical bond and

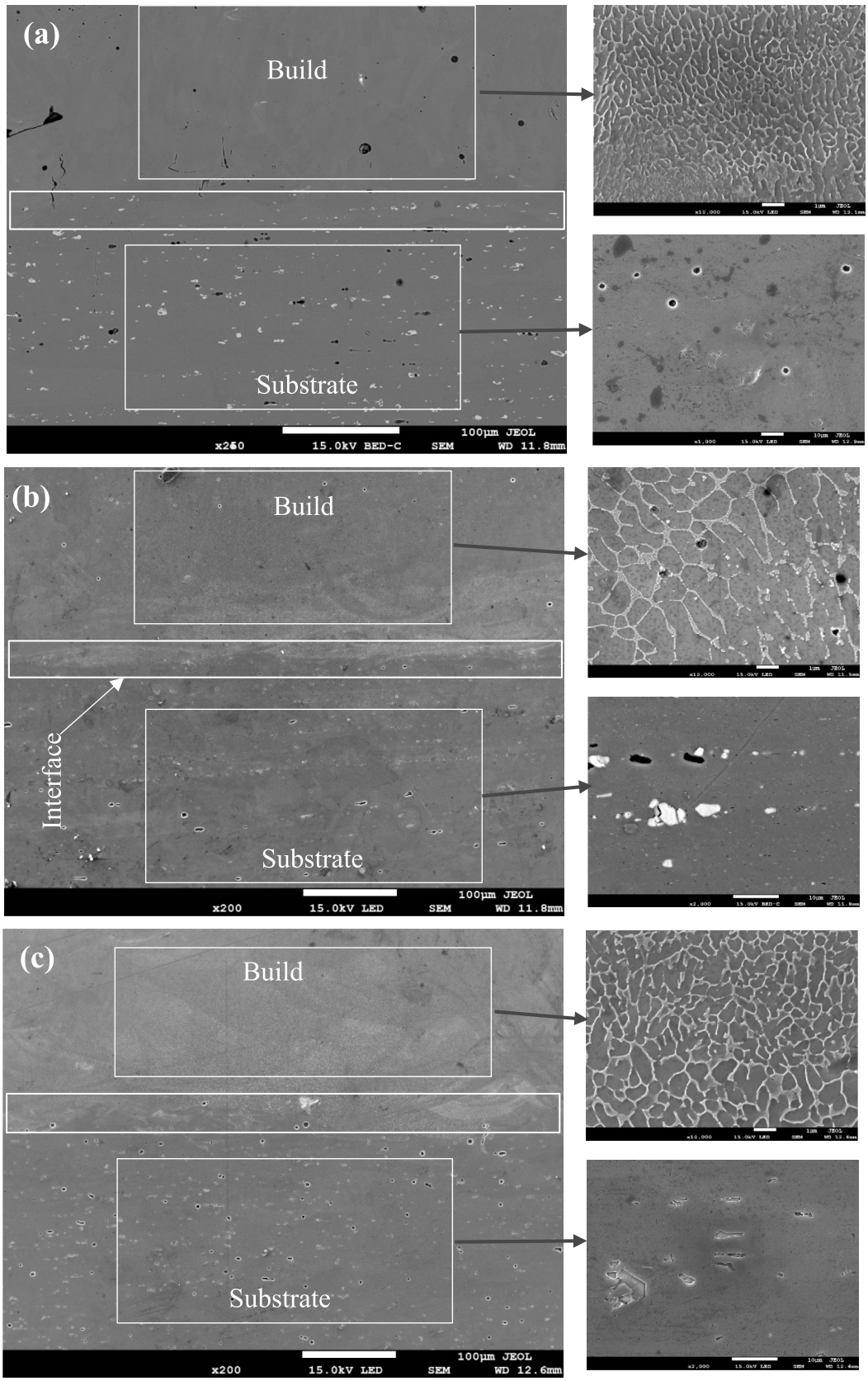

Fig. 3 SEM micrographs of hybrid samples. **a** Sample A (Al–Si7/Al 6061), **b** Sample B (Al–Si10/Al 6061), and **c** Sample C (Al–Si7/Al 5083) before corrosion

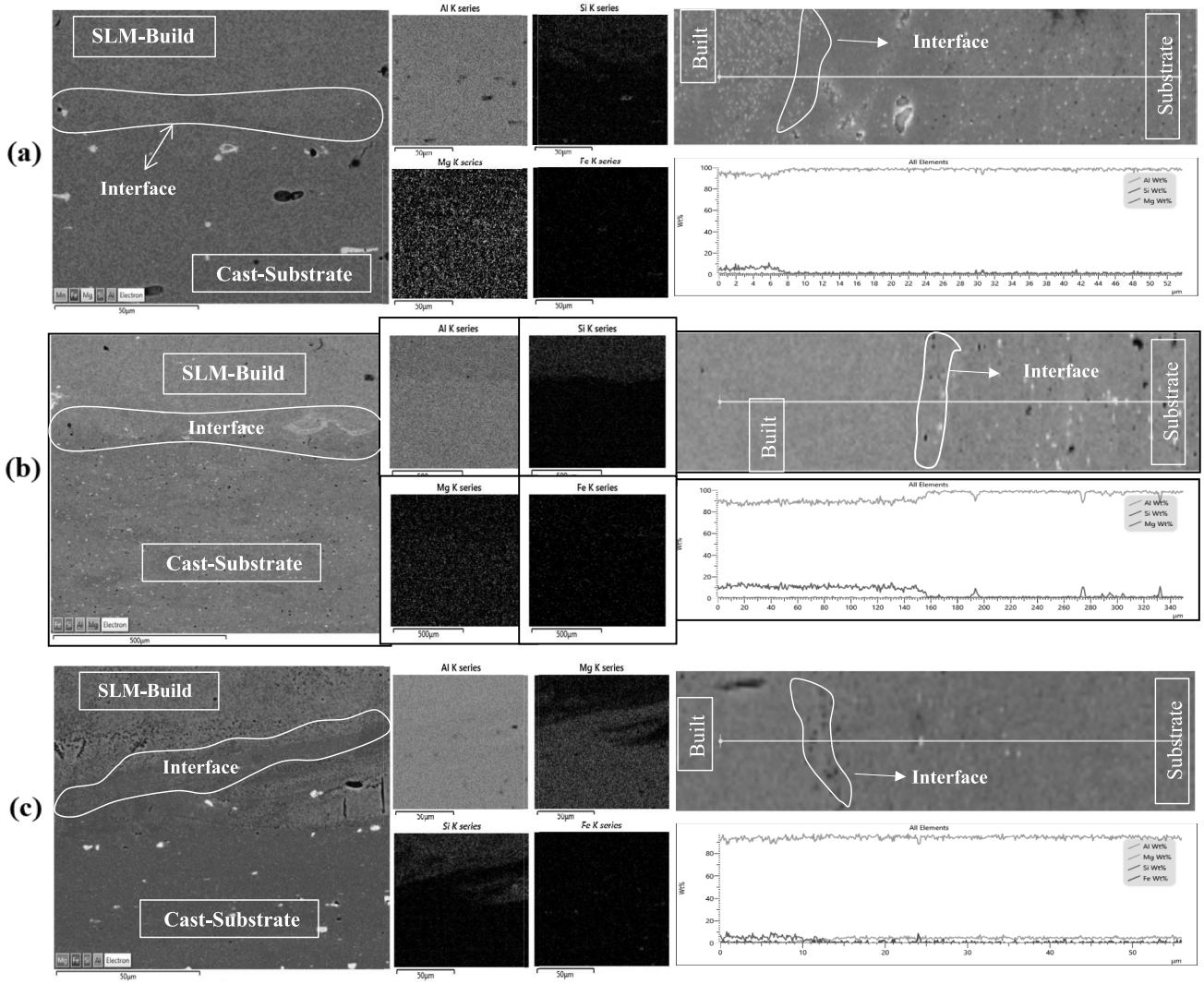

Fig. 4 SEM–EDS maps and line scan profiles across the build–substrate interfaces of hybrid aluminium alloys: **a** Sample A, **b** Sample B, and **c** Sample C. Each includes elemental distribution maps (Al, Si, Mg, Fe), a line scan SEM micrograph, and corresponding EDS profiles

moderate well-matched chemical and thermal correlation between the two sections. This is ascribed to the proper chemistry of the built and substrate materials, thus restricting segregation and improving interface quality.

Sample B similarly uses a cast Al 6061 substrate, but the built section is Al-Si10, producing a higher silicon-rich structure in the zone. The built section consists of a denser eutectic silicon network, as shown in Fig. 3b, which possibly enhances hardness but increases the chemical mismatch with the interface. Despite the slightly close similarity in the alloying systems, the variation in the silicon composition between the built region and substrate (10 wt% vs. < 1 wt%) initiates a sharper elemental gradient at the interface, consequently leading to microsegregation and galvanic coupling when the component is inserted or exposed to a harsh environment like HCl. Figure 4b shows SEM–EDS line evaluation across the hybrid structure interface. A discrete variation in silicon composition is detected at the transition phase, signifying a concentration gradient between the SLM-Build and cast substrate of Sample B. Despite the fact that the microstructural bond still sustains its solidity, the sharper changes zone can potentially incorporate the localized residual stress and phase mismatch, making the hybrid Sample B more prone to corrosion [22].

Figure 3c shows Sample C, composed of an Al-Si7 built alloy with a cast Al 5083 substrate. The built zone is the same as Sample A's, with a fine and uniformly distributed eutectic Si network. Although the substrate in this hybrid is different – Al 5083, which is a magnesium-rich cast alloy, and its microstructure shows that large dendritic α-Al grains are identifiable, interspersed with Mg-rich intermetallics like Mg_2Si and Al_6Mn (Fig. 5). Some levels of casting defects,

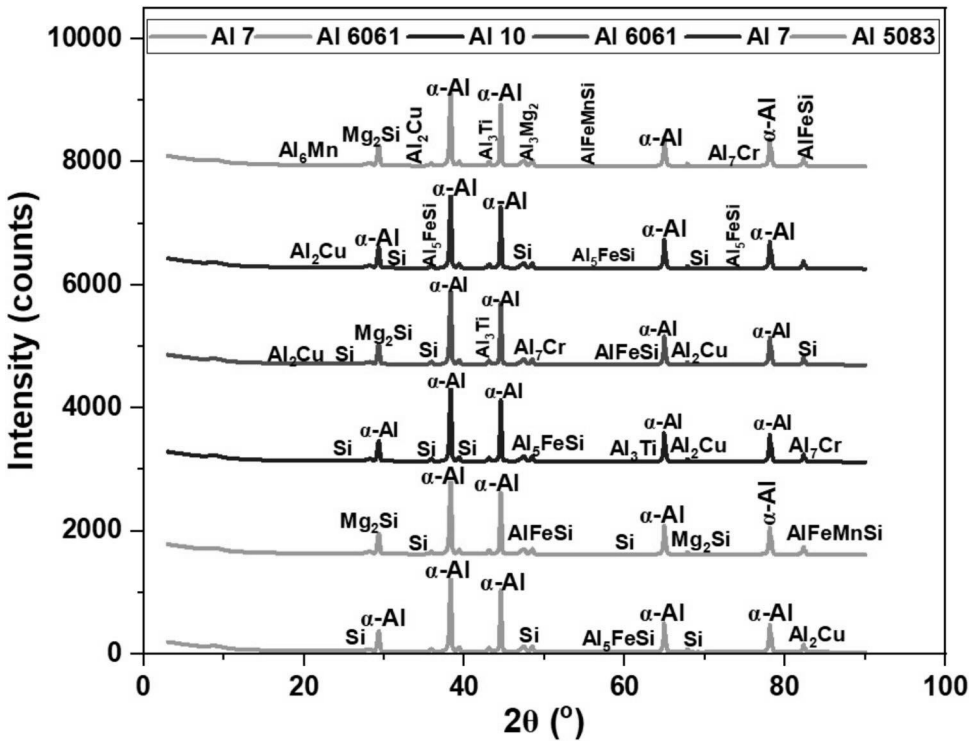

Fig. 5 XRD patterns of hybrid aluminium alloy samples, distinctly showing phase variations between the built and substrate regions of Sample A (Al–Si7/Al 6061), Sample B (Al–Si10/Al 6061), and Sample C (Al–Si7/Al 5083)

like porosity, are present. Despite the intrinsic variations in chemistry, the interface shows well-fused and minimal defect features. The smooth metallurgical transition emanates from the well-matched thermal activity between the Al Si7 build and Mg-containing Al 5083 substrate. The lesser elemental differences across the interface assist in reducing the accumulation of segregation and stress at the fusion region. The SEM–EDS line scan analysis across the interface of the hybrid structure of Sample C, as shown in Fig. 4c, reveals a high silicon concentration gradient at the built region, which can induce galvanic mismatch with the cast substrate. However, this impact can be partially counteracted by the presence of appreciable amounts of magnesium, contributing to film stability and corrosion mitigation at the interface [23].

Furthermore, the XRD results (Fig. 5) reveal that all the aluminium alloys are mainly composed of an α-Al matrix, along with silicon and a variety of secondary intermetallic compounds such as Mg_2Si, Al_5FeSi, Al_2Cu, and Al_3Mg_2. The appearance of Al_3Ti and Al_7Cr phases in Al 10 and Al 5083 reflects deliberate microalloying additions [24]. In the case of Al 5083, the presence of AlFeMnSi points to the fact that manganese plays a key role in stabilizing the intermetallic structures.

Overall, the as-fabricated microstructures of the hybrid samples exhibit that the SLM process produces refined built-zone characteristics with uniform silicon distribution, while the cast substrates show coarse dendritic structures and casting defects. The quality and stability of the built–substrate interface differ with some level of compositional disparity, consequently influencing potential galvanic performance. Remarkably, Sample C benefits from a combination of a compatible interface and corrosion-shielding Mg and Cr-enriched 5083 substrate. Sample A follows with a balanced microstructure and good interface integrity. On the other hand, Sample B, despite its fine-built structure, can be more susceptible because of sharper compositional variation and pores. These microstructural examinations provide background information on electrochemical behaviour in the following corrosion evaluation.

3.2 Open circuit potential

Figure 6 reveals the open circuit potential (OCP) profiles of the hybrid aluminium samples designated Sample A (Al–Si7 built on Al 6061), Sample B (Al–Si10 built on Al 6061), and Sample C (Al–Si7 built on Al 5083). The objective is to further determine the electrochemical stability of hybridized aluminium structures, especially under aggressive acidic environments.

The potential of all three samples commences around − 0.831 V, indicating an active metal surface exposure to chloride attack. As immersion duration progresses, their potentials shift positively, reflecting the development and thickening of passive oxide layers (surface passivation), specifically aluminium oxide (Al_2O_3), which minimizes further corrosion [25]. Sample C depicts the highest stable and noble OCP, with distinctive stabilization between 3000 and

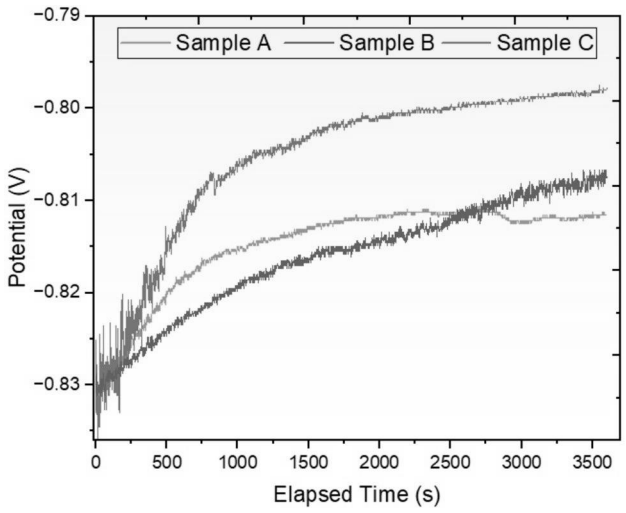

Fig. 6 Open circuit potential (OCP) profiles of hybrid aluminium alloy samples (Sample A: Al–Si7 on cast Al 6061, Sample B: Al–Si10 on cast Al 6061, Sample C: Al–Si7 on cast Al 5083) immersed in a 1 M HCl solution. The plot shows the potential stabilization behaviour over time, pinpointing the galvanic interaction and corrosion tendencies at the built–substrate interfaces

3600 s. This outcome reflects enhanced electrochemical compatibility between the Al-Si7 built layer and the Al 5083 substrate. The stabilized and noble final potential indicates steady passive film formation, potentially aided by the existence of Mn and Mg in the substrate (Al 5083 alloy), which improves the shielding oxide film stability and durability [26].

Although Sample B reached a comparative noble potential (~–0.811 V), its stabilization is delayed and inconsistent, from 2500 to 3600 s. The higher composition of 10wt% Si in the built layer enhances passive film formation by decreasing pit promotion sites and developing metallurgical stability. But the galvanic mismatch between the Al-Si10 built region and the Al 6061 substrate initiates an electrochemical galvanic gradient force that promotes localized corrosion at the interface. This consequently produces a slower stabilization and potential fluctuation. This performance aligns with the discoveries by Wu et al. (2023), who highlighted that despite the fact that Si content generally improves corrosion resistance, galvanic mismatches in dissimilar alloys can change these benefits by disrupting the passive film and thus make Sample B relatively more susceptible despite its noble potential [27].

Contrastingly, Sample A, which has a similar substrate (Al 6061) as Sample B but lesser Si content (7 wt%) in the built layer, stabilizes earlier, from 2000 and 3600 s at a bit more negative potential (~–0.814 V). The close compositional correlation between the built and substrate alloys decreases galvanic gradients and leads to smoother passivation. In spite of its fair, less noble potential in contrast to Sample B, its rapid and steadier stabilization indicates more perfect overall electrochemical compatibility. This indicates a major aspect of hybrid alloy design that reducing potential gradient across interfaces can be highly efficient in corrosion resistance, depending on each region's nobility [28]. Notably, the outcomes pinpoint that galvanic interactions at the built–substrate interface hugely impact the overall corrosion performance of the hybrid samples more than the built material alone or its substrate counterparts, as well as the bulk characteristics of the constituent alloys. This is evident in Sample A outpacing Sample B, despite having a greater Si concentration. When the built region is greater in Si than the substrate, as seen in Sample B, there will be a huge disparity in the anodic–cathodic site, escalating galvanic currents that restrict passivation and aggravate localized attack [29]. On the other hand, Sample A's comparatively closer Si content to the substrate gives less galvanic differential, inducing earlier stabilization.

Therefore, the corrosion resistance hierarchy based on OCP behaviour is: Sample C > Sample A > Sample B. Although Sample B reaches a more noble final value, its delayed and inconsistent stabilization nullifies its practical corrosion resistance [10, 12, 15]. Sample A, although moderately more negative, stabilizes earlier and more consistently than Sample B. Sample C adds both a steady and the noblest potential, establishing it as the most corrosion-resistant configuration among the hybrids examined.

3.3 Potentiodynamic polarization

The potentiodynamic polarization (PDP) behaviour of the hybrid aluminium samples—Sample A (Al–Si7 deposited on Al 6061), Sample B (Al–Si10 deposited on Al 6061) and Sample C (Al–Si7 deposited on Al 5083) were evaluated in 1 M HCl, aimed to give insight to their corrosion resistance, particularly at the interface between the built layer and the substrate. The PDP curves shown in Fig. 7 reveal vital electrochemical characteristics of the samples. Also, some parameters that were achieved by Tafel fitting, such as corrosion potential (E_{corr}), corrosion current density (I_{corr}), and Tafel slopes (B_a for anodic and B_c for cathodic reactions), which collectively give insight into the corrosion rate, are summarized in Table 2.

The corrosion potentials of the three samples (E_{corr}) fall within the active corrosion domain, signifying the vulnerability of aluminium to dissolution in HCl environments. This performance is consistent with the known reactivity of aluminium in chloride-containing solutions. Among the samples, Sample C performed excellently with the least negative Ecorr value (− 768.78 mV) and the lowest corrosion current density (I_{corr} = 3.904 mA/cm^2), pointing to a comparatively more noble electrochemical response and slower corrosion kinetics. This also indicates enhanced stability at

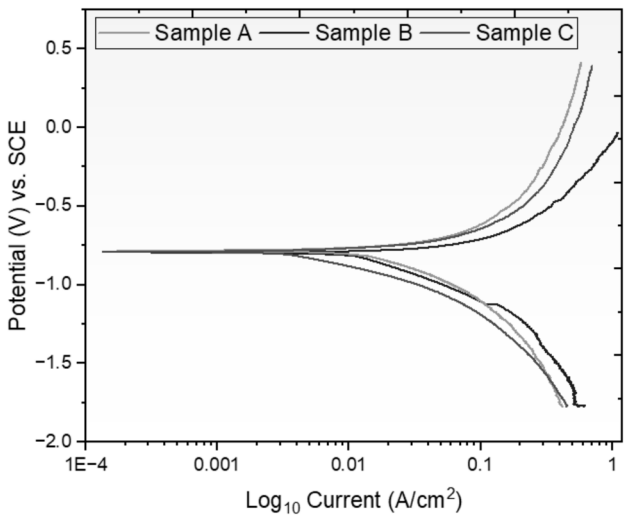

Fig. 7 PDP curves of hybrid aluminium samples in a 1 M HCl solution: Sample A (Al–Si7/6061), Sample B (Al–Si10/6061), and Sample C (Al–Si7/5083)

the built-substrate interface for this specific hybrid configuration. Conversely, Sample B showed the most negative E_{corr} and the highest I_{corr}, reflecting its greater susceptibility to corrosion under the examined conditions.

Sample A displayed better corrosion resistance than B, as evidenced by its lower corrosion current density (14.958 vs. 29.619 mA/cm^2) and reduced corrosion rate (1.61 vs. 3.17 mm/year). Notably, this happened in spite of Sample B having a greater silicon amount. This outcome relates to findings in the literature, which state that an elevated silicon proportion can incorporate greater electrochemical potential variations at the built-substrate interface, thus initiating galvanic corrosion when paired with a dissimilar substrate [28]. The comparatively steady behaviour of Sample A can hence be ascribed to a more balanced potential distribution across the interface, which aids in minimizing localized corrosion activity. The superiority of Sample C, though sharing a similar built composition with Sample A, can be credited to the presence of the Al 5083 substrate, which comprises a greater magnesium proportion (4.9 wt%) known to form protective Mg-rich passive layers. This mitigates the severity of galvanic coupling and enhances the stability of passive film formation at the interface. Such behaviour is consistent with observations reported by Lopez et al. [30], where Al–Mg-based substrates were shown to promote passivation in hybrid additive manufacturing systems.

The potentiodynamic polarization (PDP) curves display distinct cathodic and anodic branches, each representing an important portion of the corrosion kinetics. The cathodic branch, located to the left of the corrosion potential (Ecorr), corresponds primarily to the hydrogen evolution reaction in the acidic HCl environment [29]. The cathodic Tafel slope (Bc) provides insight into the kinetics of this reaction; a steeper slope implies reduced cathodic activity and, consequently, improved corrosion resistance [31]. Sample C exhibited the highest Bc value (0.100 V/dec), demonstrating slower cathodic kinetics and better interfacial protection. On the other hand, the anodic branch, positioned to the right of E_{corr}, represents the active dissolution of aluminium. The anodic Tafel slope (Ba) reflects the rate at which this oxidation process occurs, with higher values substantiating slower anodic reactions. Again, Sample C demonstrated favourable performance with 47.019 mV, implying moderated anodic dissolution likely influenced by passive film formation promoted by the Mg-rich 5083 substrate. Taken together, the combination of a lower I_{corr}, higher Tafel slopes, and a more noble E_{corr} in Sample C once again confirms its superior electrochemical stability and corrosion resistance at the built–substrate interface.

Considering all evaluated parameters, corrosion potential (E_{corr}), corrosion current density (I_{corr}), Tafel slopes (Ba and Bc), and corrosion rate, the corrosion resistance of the hybrid aluminium samples follows a similar order as reported in the OCP. This trend highlights the critical influence of galvanic compatibility between the built and substrate materials, the silicon content in the alloy, and the presence of alloying elements such as magnesium and chromium in the substrate. In particular, the improved performance of Sample C underlines the beneficial role of Mg- and Cr-enriched 5083 substrates in promoting passive film stability and mitigating interfacial corrosion.

Table 2 Electrochemical parameters obtained from potentiodynamic polarization (PDP) tests of hybrid aluminium samples in a 1 M HCl. The table summarizes the corrosion potential (Ecorr), corrosion current density (Icorr), anodic and cathodic Tafel slopes (Ba and Bc)

Sample	Built–Substrate Configuration	E_{corr} (mV)	I_{corr} (mA/cm^2)	Ba (mV)	Bc (mV)	EW (g/equiv)	Corrosion Rate (mm/year)
Sample A	Al–Si7/Al 6061	−728.504	14.958	88.36	368.976	0.0889	1.61
Sample B	Al–Si10/Al 6061	−799.55	29.619	150.67	620.831	0.0883	3.17
Sample C	Al–Si7/Al 5083	−768.78	3.904	47.019	217.397	0.0889	0.42

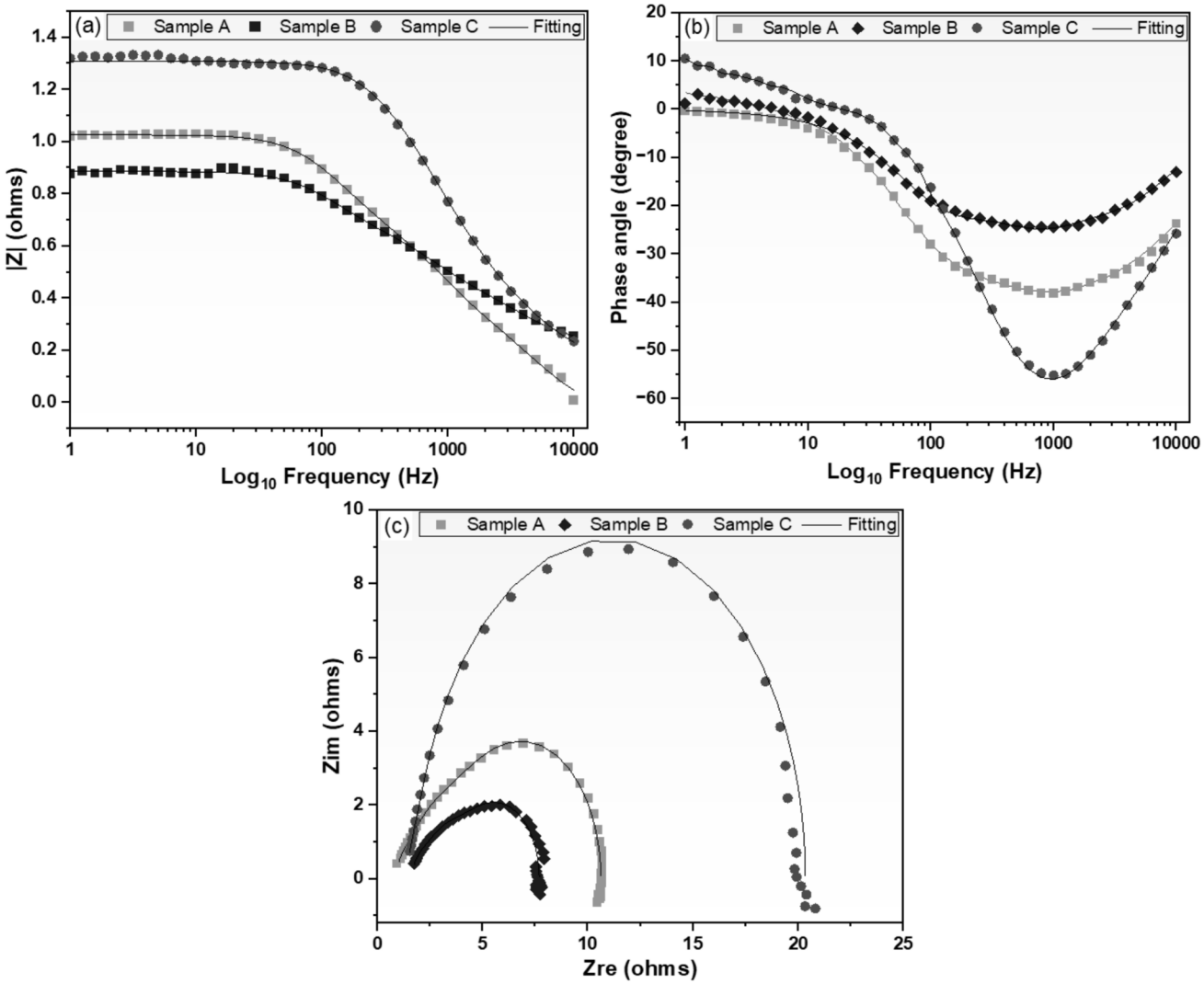

Fig. 8 EIS characterization of hybrid aluminium configurations of Sample A (Al–Si7/6061), Sample B (Al–Si10/6061), and Sample C (Al–Si7/5083) in a 1 M HCl solution: **a** Bode magnitude plot, **b** Phase angle plot, and **c** Nyquist plot

3.4 Electrochemical impedance spectroscopy

Electrochemical impedance spectroscopy was further employed to examine the corrosion behaviour of the hybrid aluminium alloy structures. The experimental data are stated in the form of Bode (|Z| and phase angle vs. frequency) and Nyquist plots for Samples A (Al–Si7/Al 6061), B (Al–Si10/Al 6061), and C (Al–Si7/Al 5083), as shown in Fig. 8a–c.

Figure 8a illustrates that the impedance modulus (|Z|) declines with increasing frequency for all samples. At low frequencies (< 10 Hz), the |Z| depicts the polarization resistance, which is hugely connected with the corrosion resistance of the materials [32, 33]. Among the samples, Sample C consistently exhibits the optimum impedance values across the frequency spectrum, implying a robust barrier to ionic conduction and electron transfer. Such improved behaviour arises from the intrinsic chemistry of Al 5083, as some of its element content favours both passive layer stability and the strengthening of the alloy matrix, which together enhance durability in aggressive chloride solutions [16]. A moderate impedance value was depicted by Sample A, signifying an appreciable protective passive film. However, it is less stable when compared to Sample C. The relatively lower impedance modulus observed for Sample B indicates the presence of a more porous or less protective oxide layer, facilitating greater ionic transport across the interface [25]. The tendency is attributed to the higher silicon fraction in the Al–Si10 alloy, which disrupts the continuity of the protective oxide layer and hinders the development of a stable passive film. Previous studies have shown that silicon-rich phases can reduce corrosion resistance by promoting microgalvanic interactions with the surrounding aluminium

matrix, thereby accelerating localized degradation processes [21, 29]. In this case, the substrate had most of its surface oxide disintegrated, as shown in the SEM image (Fig. 10).

Figure 8b displays the phase angle (θ) as a function of frequency, which reflects the capacitive nature of the surface oxide layer. A high, broad phase angle close to − 90° indicates ideal capacitive behaviour and a protective passive layer [34]. Sample C again demonstrates the most capacitive response, with a broad and deep phase minimum of around − 55°, implying a homogeneous and compact oxide structure [35]. This behaviour aligns with past findings that magnesium-enriched aluminium substrates promote thicker and more protective oxide layers [36]. In contrast, Sample A reaches a maximum phase angle of around –40°, while Sample B shows a phase minimum of only − 30°, indicating a thinner or more defective oxide layer. Sample A, with moderate phase values (− 40°), indicates intermediate corrosion resistance, likely due to its more balanced Si content (7 wt%) and metallurgical compatibility between the build and the substrate.

The Nyquist plots (Fig. 8c) provide further insight into the electrochemical mechanisms operating within the samples. The semicircular diameter is related proportionally to polarization resistance. Sample C features a large, well-defined semicircle, showing evidence of high charge transfer resistance and low corrosion rate. Conversely, Sample B shows the smallest semicircle, consistent with its lower Bode impedance and higher corrosion current (as corroborated by PDP data). Sample A exhibits moderate arc size, reinforcing its intermediate behaviour. The improved performance of Sample C can also be partially attributed to better metallurgical bonding at the SLM/substrate interface, which contributes to reduced porosity and fewer initiation sites for corrosion [30] and other favourable conditions, as previously stated.

3.4.1 Electrochemical impedance spectroscopy analysis of equivalent circuit parameters

The EIS data for three hybrid aluminium alloy samples, Sample A, Sample B, and Sample C, were fitted to an equivalent circuit consisting of resistive and capacitive elements: Rs, R_1, R_2, R_3, and C_1, C_2, and C_3. These elements represent the electrochemical characteristics at various surfaces of the hybrid systems, consistent with the widely accepted R(Q(R(Q(RQ))) model for layered passive films [37]. This circuit model was selected based on the shape of the Bode and Nyquist plots, which reveal the presence of multiple capacitive behaviours and diffusion-related processes across the built–substrate interface.

As shown in the EIS Plot (Fig. 8), the simulated curves (fitting) show good agreement with the experimental data across all frequency domains, corroborating the suitability of the chosen model (Fig. 9). The extracted fitting parameters are summarized in Table 3. Here, the solution resistance – Rs, for all samples, values were relatively low, as expected in an aqueous chloride environment (0.97–1.71 Ω), confirming effective ionic conduction in the test environment [38], with Sample A showing the lowest Rs (0.9733 Ω). The C_1, C_2, and C_3 are the constant phase elements (CPEs) accounting for non-ideal capacitive behaviour at different depths of each layer. Particularly, C_1 depicts the outer passive layer, C_2 represents the bulk of the passive film, and C_3 is associated with deeper diffusion or interfacial polarization phenomena [39]. The higher capacitance values often highlight a thinner or more defective passive film, which is typically less protective. Sample C recorded the lowest values for both C_1 (6.0223×10^{-5} F), C_2 (7.1992×10^{-5} F), and C_3 (2.4982×10^{-4} F) and also demonstrated the highest corresponding resistance values. This combination implies the presence of a structured and efficient protective passive layer, likely influenced by the good compositional chemistry between the builts and substrate [38]. In comparison, Sample B exhibited the highest capacitance values, as reflected in the sample's overall poorer electrochemical performance [40].

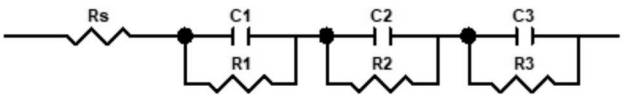

Fig. 9 Equivalent electrical circuit used to model the electrochemical impedance performance of the system

The resistance components R_1, R_2, and R_3 in the equivalent circuit model represent different electrochemical processes across the hybrid structure. R_1 generally corresponds to the outer layer's resistance, R_2 the intermediate layer or alloy interface, and R_3 represents diffusion-related resistance or slower long-term reactions [38]. Sample C again stands out, showing substantially higher resistance values across all three layers: $R_1 = 0.827$ Ω, $R_2 = 7.5$ Ω, and $R_3 = 10.38$ Ω. This reflects a robust barrier effect and a more stable corrosion system. Meanwhile, Sample B demonstrated the lowest resistance values ($R_1 = 0.500$ Ω, $R_2 = 1.644$ Ω, $R_3 = 3.503$ Ω), confirming weaker corrosion protection and a more active, ongoing degradation process. Sample A exhibited a balanced level of corrosion resistance, aligning well with its mid-range behaviour observed in complementary electrochemical evaluations.

These impedance fitting results are in strong agreement with earlier observations from potentiodynamic polarization (PDP) and Bode phase angle plots. The hybrid structure (Sample C), which consistently demonstrated the most noble corrosion behaviour, is supported by the broader and deeper phase angle minimum and higher impedance magnitude. According to the literature, higher polarization resistance ($R_1 + R_2 + R_3$) and sustained capacitive behaviour over a wide frequency range are reliable indicators of passive film integrity and overall corrosion resistance [41].

Table 3 Equivalent circuit fitting parameters obtained from EIS data for the hybrid aluminium alloys: Sample A (Al–Si7/Al 6061), Sample B (Al–Si10/Al 6061), and Sample C (Al–Si7/Al 5083). The fitted values correspond to the circuit model comprising solution resistance (Rs), charge transfer resistances (R_1, R_2, R_3), and constant phase elements (C_1, C_2, C_3) representing the electrochemical interfaces and corrosion behaviour of the samples

Sample	Rs (Ω)	C_1 (F)	R_1 (Ω)	C_2 (F)	R_2 (Ω)	C_3 (F)	R_4 (Ω)
Sample A	0.9733	6.5198×10^{-5}	0.7139	1.1568×10^{-4}	2.193	4.4906×10^{-4}	6.765
Sample B	1.706	8.8078×10^{-5}	0.500	1.6258×10^{-4}	1.644	5.5292×10^{-4}	3.503
Sample C	1.500	6.0223×10^{-5}	0.8269	7.1992×10^{-5}	7.5	2.4982×10^{-4}	10.380

3.5 Microstructural Evolution After Electrochemical Exposure

The corrosion morphology of the hybrid aluminium alloy samples following their immersion in HCl solution was examined using SEM and EDS analyses, as presented in Fig. 10. Distinct variations in surface depletion were observed among the samples, characterized by differences in pit formation, crack propagation, and corrosion product accumulation. These differences are closely associated with the compositional interplay between the selectively laser-melted (SLM) build layers and their respective substrate alloys. Each hybrid system responded uniquely to the corrosive environment, reflecting the impact of microstructural characteristics and elemental dispersal on its corrosion resistance performance.

Figure 10a depicts the SEM image of Sample A; it reflects moderate surface depletion marked by visible cracking and non-uniform spread of corrosion products, specifically concentrated at the interface between the SLM-built region and the cast substrate and more noticeably across the substrate region. These corrosion products are a reflection of galvanic mismatch between the two surfaces, owing to the high silicon concentration in the build rather than the substrate. Also, the cracked zones are a result of the localized failure of the passive aluminium oxide layer, worsened by inherent microstructural variations and potential residual thermal stresses linked with the SLM procedure [10, 25]. Corresponding EDS spectra justify a noticeable reduction in aluminium concentration in corroded sections alongside a relative rise in oxygen levels, reflecting the formation of hydroxide ($Al(OH)_3$) or aluminium oxide (Al_2O_3) as a corrosion by-product. Although these oxides give a partial shield, their inconsistent development appears to have left some sections susceptible to localized corrosion and crack propagation. The minimal detectable chlorine in the examined sections indicates that chloride entrapment did not cause an appreciable deterioration and that the deterioration mechanism is likely driven by passive inconsistency other than by harsh chloride ion interaction. This further demonstrates that the few chlorides left on the surface after exposure pointed to the involvement of structural characteristics in influencing the corrosion performance [42].

For Sample B, the surface damage caused by corrosion was more destructive than that of Sample A. The SEM image (Fig. 10b) exhibits some levels of pitting, interconnected cracks, and deep corrosion trenches, indicative of highly aggressive localized corrosion. The EDS analysis further validates these observations by showing increased oxygen signals in severely depleted regions, hence demonstrating the development of Al_2O_3 or $Al(OH)_3$ as corrosion products. Some of the peaks sparingly indicate the existence of chlorine. However, the featured pitting and crack spread patterns demonstrated that chloride ions played a role in the first passive film deterioration [43]. This mechanism is synonymous with the study established by Shi and Andrej, where Cl^- ions initiate a localized attack in a component immersed in a solution containing chlorine, while the final corrosion products largely comprise $Al(OH)_3$ or Al_2O_3 [44]. Overall, the combination of silicon-induced galvanic impacts, compositional differences across the interface, and chloride-assisted passivation breakdown adds to the poor corrosion performance in Sample B.

The SEM micrograph of Fig. 10c reveals a surface morphology characterized by the least surface deterioration of relatively uniform corrosion features with minimal cracking and the absence of deep pits or severe material loss. A continuous layer of corrosion products covers both the build and substrate regions, corroborating that the corrosion mechanism was more uniform and less localized compared to Samples A and B. This enhanced corrosion behaviour can be largely attributed to the Al 5083 substrate, which is alloyed with magnesium, a known enhancer of passivation activity in aluminium alloys [44]. Magnesium can promote the formation of protective surface films such as $Mg(OH)_2$ and mixed Al–Mg hydroxides, which improve the integrity of the oxide layer and mitigate harsh chloride-induced attacks [20]. The accompanying EDS spectra confirm this observation, showing elevated oxygen levels along with stable aluminium peaks, which point to the development of a compact and adherent oxide/hydroxide film. The absence of chlorine spectra in both the build and substrate regions further supports the idea that this corrosion layer effectively resisted Cl^- ion ingress, thus decreasing further depletion and pitting activity [43].

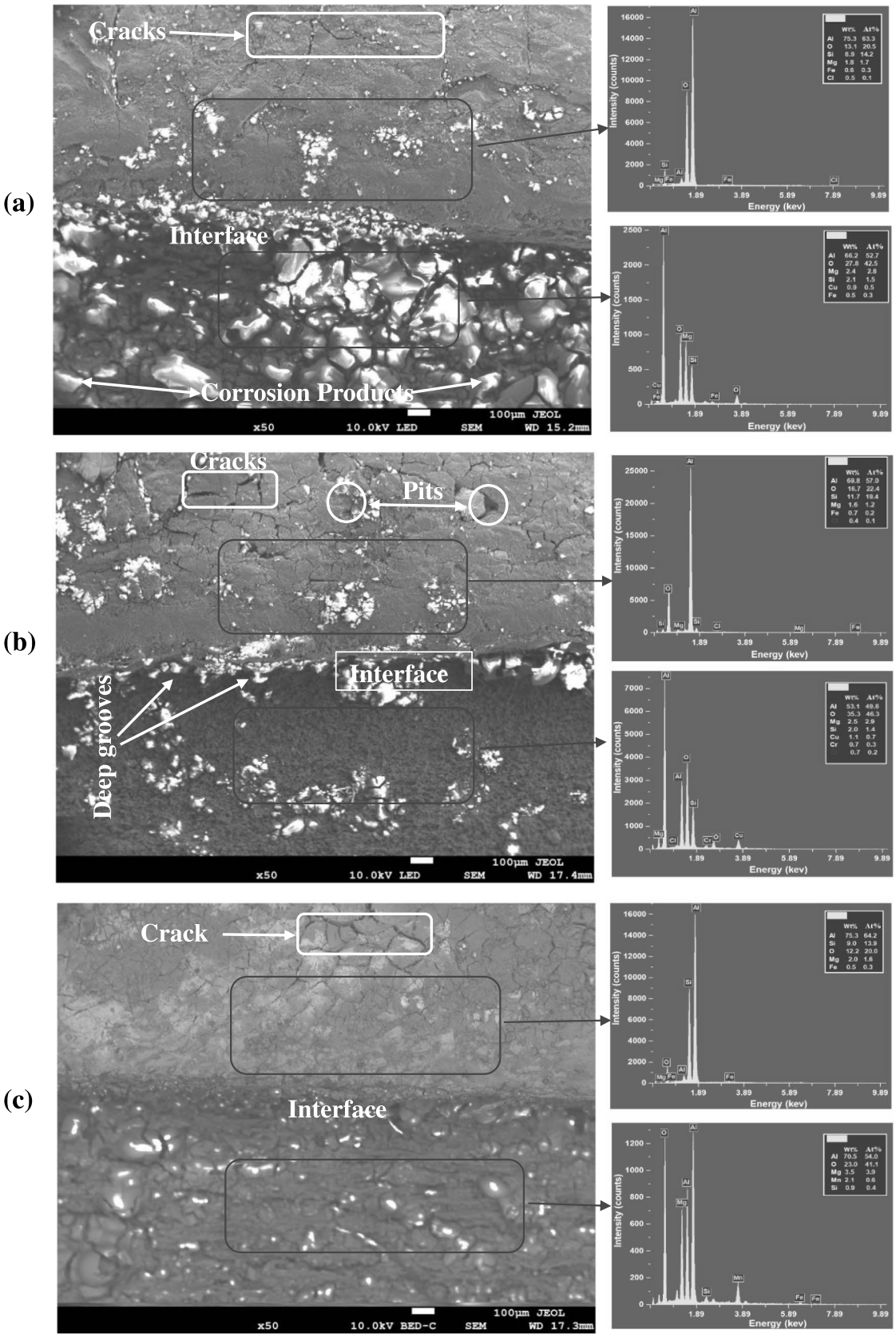

Fig. 10 SEM micrographs and corresponding EDS spectra of the corroded hybrid aluminium alloy samples following their immersion in 1 M HCl solution: **a** Sample A (Al–Si7/Al 6061), **b** Sample B (Al–Si10/Al 6061), and **c** Sample C (Al–Si7/Al 5083)

4 Conclusion

This study explored the corrosion performance of hybrid aluminium alloy structures developed by merging selective laser melting (SLM) with conventional casting. Three hybrid configurations were examined using electrochemical techniques, including OCP, EIS, and PDP, and surface and microstructural examinations were conducted before and after exposure to 1 M HCl solution. The outcomes from this work reveal that the corrosion resistance of the samples was consistently ranked as Sample C > Sample A > Sample B. Sample C was significantly the best, due to its Mg-enriched cast substrate and uniform, refined microstructure, which promoted the formation of a stable passive film. Contrastingly, the higher Si content in the SLM region specifically for Sample B encouraged the formation of cathodic intermetallics, which accelerated localized corrosion along the interface. SEM/EDS analyses further corroborated that hybrids with smoother compositional transitions and well-engineered interfaces corroded more uniformly.

Overall, the corrosion response of hybrid aluminium systems is strongly influenced by how well the interface is tailored, most importantly in terms of microstructure and alloy composition transition between the two regions. Together, the electrochemical data and surface observations highlight the importance of designing hybrid configurations that minimize galvanic mismatches and support long-term durability for aerospace and marine applications in aggressive service environments.

Acknowledgements The authors gratefully acknowledge the University of Johannesburg, South Africa, for its support. This research was conducted with the assistance of the Centre for Nanoengineering and Advanced Materials, University of Johannesburg.

Author contribution Samson Dare Oguntuyi: conceptualization, methodology, investigation, formal analysis, data curation, writing—original draft; Mandlenkosi G.R. Mahlobo: methodology, supervision, validation, writing—review and editing; Ngeleshi M. Kibambe: resources, data interpretation, writing—review and editing; Kasongo Nyembwe: supervision, project administration, funding acquisition, writing—review and editing. Peter M. Mashinini: visualization, experimental support, writing—review and editing. Peter Apata Olubambi: supervision, conceptual guidance, writing—review and editing.

Funding Open access funding provided by University of Johannesburg. This research is partly funded by the University Research Council.

Data availability The data that support the findings of this study are available from the corresponding author upon reasonable request. No publicly available dataset was used or generated for this research.

Declarations

Ethical approval Not applicable.

Consent to participate Not applicable.

Consent for publication Not applicable.

Conflict of interest The authors declares no competing interests.

References

1. Zhang Z, Dandu RSB, Klu EE, Cai W (2023) A review on tribocorrosion behavior of aluminum alloys: from fundamental mechanisms to alloy design strategies. Corros Mater Degrad 4(4):594–622. https://doi.org/10.3390/cmd4040031
2. Liu C, Davis A, Fellowes J, Prangnell PB, Raabe D, Shanthraj P (2022) CALPHAD-informed phase-field model for two-sublattice phases based on chemical potentials: η-phase precipitation in Al-Zn-Mg-Cu alloys. Acta Mater 226:117602. https://doi.org/10.1016/j.actamat.2021.117602
3. Tan Q, Liu Y, Fan Z, Zhang J, Yin Y, Zhang M-X (2020) Effect of processing parameters on the densification of an additively manufactured 2024 Al alloy. J Mater Sci Technol 58:34–45. https://doi.org/10.1016/j.jmst.2020.03.070
4. Zhao J et al (2024) Corrosion behavior of the 2024 aluminum alloy in the atmospheric environment of the South China Sea islands. Coatings 14(3):331. https://doi.org/10.3390/coatings14030331
5. Chen B-Q, Liu K, Xu S (2024) Recent advances in aluminum welding for marine structures. J Mar Sci Eng 12(9):1539. https://doi.org/10.3390/jmse12091539
6. Gao L, Zhang H, Zhi H, Wang H, Dong P (2025) Corrosion characteristics and corrosion depth predicted of rolled/laser metal deposition additive manufactured Ti-6Al-4V joints. Mater Today Commun 44:111897. https://doi.org/10.1016/j.mtcomm.2025.111897
7. Lehmhus D et al (2025) Combining metal additive manufacturing and casting technology: high performance cooling channels for electric powertrain components. Adv Eng Mater 27:2500445. https://doi.org/10.1002/adem.202500445
8. P. O. Omoniyi *et al.*, Corrosion behavior of laser-welded Ti6Al4V in 3.5% Wt NaCl, in *Advances in Material Science and Engineering: Selected Articles from ICMMPE 2021*: Springer, 2022, pp. 395–400.
9. Culliton D, Betts AJ, Kennedy D (2013) Impact of intermetallic precipitates on the tribological and/or corrosion performance of cast aluminium alloys: a short review. Int J Cast Met Res 26(2):65–71. https://doi.org/10.1179/1743133612Y.0000000038
10. Jiang Z, Dai X, Middleton H (2011) Effect of silicon on corrosion resistance of Ti–Si alloys. Mater Sci Eng, B 176(1):79–86. https://doi.org/10.1016/j.mseb.2010.09.006

11. Laieghi H (2024) Corrosion in laser powder bed fusion AlSi10Mg alloy. Eng Rep (Hoboken) 6(10):e12984. https://doi.org/10.1002/eng2.12984
12. Linder C, Mehta B, Sainis S, Lindén JB, Zanella C, Nyborg L (2024) Corrosion resistance of additively manufactured aluminium alloys for marine applications. NPJ Mater Degrad 8(1):46. https://doi.org/10.1038/s41529-024-00459-5
13. Safyari M, Furuta S, Khoo PL, Kobayashi M, Moshtaghi M (2025) Exceptional stress corrosion cracking resistance of additively manufactured aluminum alloys in simulated marine environments. Mater Des. https://doi.org/10.1016/j.matdes.2025.113924
14. Adapala P (2024) Understanding the effect of microstructure and composition on localized corrosion susceptibility of 6xxx aluminum alloys. NPJ Mater Degrad 8(1):52. https://doi.org/10.1038/s41529-024-00461-x
15. Fathi P et al (2021) Corrosion performance of additively manufactured bimetallic aluminum alloys. Electrochim Acta 389:138689. https://doi.org/10.1016/j.electacta.2021.138689
16. Azar AS, Lekatou A, Sunding MF, Graff JS, Tzima N, Diplas S (2021) Corrosion performance and degradation mechanism of a bi-metallic aluminum structure processed by wire-arc additive manufacturing. NPJ Mater Degrad 5(1):26. https://doi.org/10.1038/s41529-021-00175-4
17. H. Fan, A. Witvrouw, F. Wolf-Monheim, R. Souschek, and S. Yang, Hybrid additive manufacturing of cost-effective automobile parts by die-casting (AlSi7Mg0. 3 (A356)) and selective laser melting (AlSi7Mg0. 5 (A357))—effects of substrate surface treatments on bimetallic interface bonding quality, 2022. https://doi.org/10.31219/osf.io/exbsd
18. ZainElabdeen IH, Ismail L, Mohamed OF, Khan KA, Schiffer A (2024) Recent advancements in hybrid additive manufacturing of similar and dissimilar metals via laser powder bed fusion. Mater Sci Eng A. https://doi.org/10.1016/j.msea.2024.146833
19. Schuster M, De Luca A, Widmer R, Maeder X, Leinenbach C (2022) Processability, microstructure and precipitation of a Zr-modified 2618 aluminium alloy fabricated by laser powder bed fusion. J Alloys Compd 913:165346. https://doi.org/10.1016/j.jallcom.2022.165346
20. Escalera-Lozano R, Pech-Canul MI, Pech-Canul MA, Montoya-Dávila M, Uribe-Salas A (2010) The role of Mg 2 Si in the corrosion behavior of Al-Si-Mg alloys for pressureless infiltration. Open Corrosion Journal 3:73–79. https://doi.org/10.2174/1876503301003010073
21. Ikeuba AI et al (2024) A review of the electrochemical and galvanic corrosion behavior of important intermetallic compounds in the context of aluminum alloys. RSC Adv 14(43):31921–31953. https://doi.org/10.1039/D4RA06070A
22. Kianfar S, Aghaie E, Stroh J, Sediako D, Tjong J (2021) Residual stress, microstructure, and mechanical properties analysis of HPDC aluminum engine block with cast-in iron liners. Mater Today Commun 26:101814. https://doi.org/10.1016/j.mtcomm.2020.101814
23. Korjenic A, Blohm L, Scully JR (2024) Electrochemical evaluation of Mg and a Mg-Al 5% Zn metal-rich primers for protection of Al-Zn-Mg-Cu alloy in NaCl. Corrosion 80(8):851–877. https://doi.org/10.5006/4537
24. Wang X, Liu Z, Dai W, Han Q (2015) On the understanding of aluminum grain refinement by Al-Ti-B type master alloys. Metall Mater Trans B 46:1620–1625. https://doi.org/10.1007/s11663-014-0252-3
25. Abou Shahba RM, Ibrahim AS, Shehata WAHNK, Ghanem WA (2011) Electrochemical behavior and corrosion inhibition of Al and Al-Si alloy in inorganic acidic solutions. Researcher 3(12):92–105
26. Patel S, Rao V (2023) Microstructure, mechanical properties and corrosion behaviour of Mg-Cu and Mg-Cu-Mn alloys. Materials Today: Proceedings. https://doi.org/10.1016/j.matpr.2023.06.284
27. Wu Y et al (2023) Effect of Si content on microstructures and electrochemical properties of Al-xSi-3.5 Fe coating alloy. Materials 16(23):7407. https://doi.org/10.3390/ma16237407
28. Zhang S et al (2024) Study on the microstructure and corrosion behavior of dissimilar aluminum alloy welded joints formed using laser welding. Materials 17(23):5968. https://doi.org/10.3390/ma17235968
29. Kayani SH, Ha H-Y, Kim B-J, Cho Y-H, Son H-W, Lee J-M (2024) Impact of intermetallic phases on the localised pitting corrosion and high-temperature tensile strength of Al–SiMgCuNi alloys. Corros Sci 233:112064. https://doi.org/10.1016/j.corsci.2024.112064
30. López Freixes M et al (2022) Revisiting stress-corrosion cracking and hydrogen embrittlement in 7xxx-Al alloys at the near-atomic-scale. Nat Commun 13(1):4290. https://doi.org/10.1038/s41467-022-31964-3
31. Berlanga-Labari C, Biezma-Moraleda MV, Rivero PJ (2020) Corrosion of cast aluminum alloys: a review. Metals 10(10):1384. https://doi.org/10.3390/met10101384
32. Cristoforetti A, Rossi S, Deflorian F, Fedel M (2023) On the limits of the EIS low-frequency impedance modulus as a tool to describe the protection properties of organic coatings exposed to accelerated aging tests. Coatings 13(3):598. https://doi.org/10.3390/coatings13030598
33. El-Mahdy GA, Nishikata A, Tsuru T (2000) AC impedance study on corrosion of 55% Al–Zn alloy-coated steel under thin electrolyte layers. Corros Sci 42(9):1509–1521. https://doi.org/10.1016/S0010-938X(00)00009-3
34. T. Voorhees, O. Villalpando, and V. A. Ravi, Characterization of the corrosion behavior of advanced titanium alloys in simulated physiological environments using electrochemical impedance spectroscopy, 2015: NACE, pp. 1–10, NACE-2015. https://doi.org/10.5006/C2015-06120
35. Zuo Y, Pang R, Li W, Xiong JP, Tang YM (2008) The evaluation of coating performance by the variations of phase angles in middle and high frequency domains of EIS. Corros Sci 50(12):3322–3328. https://doi.org/10.1016/j.corsci.2008.08.049
36. Wu G, Dash K, Galano ML, O'Reilly KAQ (2019) Oxidation studies of Al alloys: part II Al-Mg alloy. Corros Sci 155:97–108. https://doi.org/10.1016/j.corsci.2019.04.018
37. Yi G et al (2021) Characteristics of passive films formed on As-Cast Ti–6Al-4V in Hank's solution before and after transpassivation. Front Mater 7:640081. https://doi.org/10.3389/fmats.2020.640081
38. Kwon D, Van Pham H, Song P, Moon S (2023) Electrochemical behavior of AZ31 Mg alloy in neutral aqueous solutions containing various anions. J Electrochem Sci Technol 14(4):311–319. https://doi.org/10.33961/jecst.2023.00213
39. Orazem ME, Tribollet B (2008) Electrochemical impedance spectroscopy. New Jersey 1(906):383–389
40. Zhou L et al (2021) Microstructure, mechanical performance, and corrosion behavior of additively manufactured aluminum alloy 5083 with 0.7 and 1.0 wt% Zr addition. Mater Sci Eng A 823:141679. https://doi.org/10.1016/j.msea.2021.141679
41. Park G-D (2021) Ultra-high corrosion resistance of Al-Mg-Si film on steel sheet formed by PVD Mg coating and heat treatment. Corros Sci 192:109829. https://doi.org/10.1016/j.corsci.2021.109829
42. Xu L (2022) Structural characteristics and chloride intrusion mechanism of passive film. Corros Sci 207:110563. https://doi.org/10.1016/j.corsci.2022.110563

43. Scampone G, Timelli G (2022) Anodizing Al–Si foundry alloys: a critical review. Adv Eng Mater 24(4):2101480. https://doi.org/10.1002/adem.202101480
44. Shi Z, Atrens A (2011) An innovative specimen configuration for the study of Mg corrosion. Corros Sci 53(1):226–246. https://doi.org/10.1016/j.corsci.2010.09.016